Tellus (2003), 55A, 301–316
Printed in UK. All rights reserved

TELLUS
ISSN 0280–6495

Moist dynamics and orographic precipitation

By QINGFANG JIANG*, *University of Corporation for Atmospheric Research, Visiting scientist at Naval Research Laboratory, Monterey, CA, USA*

(Manuscript received 30 September 2002; in final form 25 February 2003)

ABSTRACT

Uniformly stratified moist flow over a Gaussian-shaped circular mountain is investigated using a nonhydrostatic mesoscale model. The focus is the interaction between flow stagnation and orographic precipitation. Two closely related issues are addressed: the effect of condensation and precipitation on mountain flow stagnation, and the influence of flow blocking and latent heat on upslope precipitation. It is demonstrated that latent heat release and precipitation can significantly delay the onset of mountain flow stagnation. The dynamical and thermodynamical nature of this modification can be qualitatively understood using the moist stability concept. However, due to the vertical variation of the moist stability, it is not possible to define a single nondimensional mountain height to describe the general nonlinearity of moist orographic flow. The effect of flow blocking and splitting on the intensity and distribution of orographic precipitation is found to be significant. For low mountains, the upslope ascent dominates and the precipitation intensity is roughly proportional to the mountain height and windspeed as predicted by both a slab model and the mesoscale model. For high mountains, this relationship breaks down because the mountain lift effect is reduced as the low level moist flow passes around the peak. An arc-shaped precipitation band forms further upstream of the peak where the terrain slope is gentle, associated with the secondary circulation forced by the upstream flow blocking/reversal. The removal of latent heat processes leads to reduced upslope lift and enhanced windward blocking, thereby reducing the maximum precipitation rates and increasing the precipitation area.

1. Introduction

Mountains exert a powerful control on the global distribution of climate, primarily by their influence on precipitation and water vapor transport. On a smaller scale, over mountainous regions with prevailing wind, precipitation is enhanced on the windward side of mountains and much reduced on the lee side. The influence of terrain on water vapor transport and precipitation has been the focus of numerous studies driven by different motivations. For example, hydrologists and glaciologist are interested in orographic precipitation because it is an important source term in river runoff prediction and snow mass balance analysis. After decades of effort, the mechanisms of orographic precipitation are still poorly understood, and the forecasting of precipitation in mountainous areas is still an elusive goal. Challenges come from a number of factors, such as the multiscale nature of complex terrain, interactions between terrain and airflow, the complex role of latent heating/cooling, and the complexity of cloud physics. So far, several orographic precipitation mechanisms have been proposed (Smith, 1979). These mechanisms can be classified into two categories: stratiform precipitation induced/enhanced by stable ascent and convection triggered/enhanced by terrain. The focus of this study is on the dynamics and precipitation associated with stable upslope ascent. The objective is to investigate moist flow stagnation and its impact on the intensity and distribution of upslope stratiform precipitation.

Numerical tools used in this study include several models of different complexity: a no-dynamics–no-microphysics slab model, a no-precipitation (hereafter, referred to as NP) model, a no-microphysics perfect

*Corresponding author address: Naval Research Laboratory, Marine Meteorology Division, 7 Grace Hopper Avenue, Monterey, CA 93943-5502 USA.
e-mail: jiang.ucar.cn@nrlmry.navy.mil

precipitation (hereafter referred to as PP) model, a no-latent-heat (hereafter, referred to as NLH) model with bulk microphysics, a no-latent-heat perfect precipitation (hereafter referred to as NLH_PP) model, and a full nonhydrostatic mesoscale model (i.e., ARPS: see section 3) with bulk microphysics.

The outline of this paper is as follows. Some relevant work is reviewed in section 2. The numerical setup is described in section 3. The moist N argument and the effect of precipitation on flow stagnation are examined in section 4. In section 5 the effect of flow splitting on the distribution and intensity of orographic precipitation is investigated. The results are summarized in section 6.

2. Historical review

As stratified airflow passes a high terrain, flow stagnation may occur over the windward slope (hereafter, referred to as stagnation point B) due to the mountain blocking effect, and aloft over the lee side due to the steepening of gravity wave (hereafter, referred to as stagnation point A). Mountain flow stagnation in the absence of moisture has been addressed in a number of studies. It has been shown that the general nonlinearity of mountain flow can be measured using the nondimensional mountain height M ($=Nh_{\mathrm{m}}/U$, where N is the buoyancy frequency, U is the cross-mountain windspeed, and h_{m} is the maximum mountain height), or mountain Froude number F_r ($=1/M$).

Several methods were proposed to determine the critical nondimensional mountain height, M_{c}, for flow stagnation. The most straightforward one is the kinetic energy argument (Sheppard, 1956), which is also well known as Sheppard's law. Based on this argument, the critical mountain height $M_{\mathrm{c}} = 1$ regardless of the mountain shape. It was pointed out by Smith (1989), however, that the pressure difference term ignored in Sheppard's law can be of the same order or larger than the kinetic energy terms. As an alternative, Smith predicted critical mountain heights for a family of bell-shaped mountains based on linear theory. For idealized topography, the critical mountain heights were also predicted by Huppert and Miles [1969, $M_{\mathrm{c}} \simeq 0.85$, two-dimensional (2-D) ridge]. More recently, this issue was addressed numerically by Smith and Grønås (1993, $M_{\mathrm{c}} = 1.1 \pm 0.1$ for a 3-D Gaussian hill and $M_{\mathrm{c}} = 1.2 \pm 0.2$ for a 3-D 3/2-power hill), and experimentally by Baines and Smith (1993, $M_{\mathrm{c}} = 1.05$, 3-D hill). The dependence of nonlinear dynamics on the nondimensional mountain height and mountain aspect ratio was investigated by Ólafsson and Bougeault (1996) and Bauer et al. (2000).

Unlike dry dynamics, moist flow dynamics has received little attention. Previous studies on moist mountain waves and orographic clouds can be classified into four categories: (i) Highly idealized treatment of moist processes, such as considered by Smith and Lin (1982). They simplified the problem by using prescribed heating/cooling functions based on observations of orographic precipitation. Linear responses to various orographic and thermal forcing were expressed in closed forms. While this approach gives us some valuable information of the thermal forcing effect, the specified passive heating/cooling sources prevent any further attempt to understand interactions between dry and wet processes. (ii) A moist static stability (N_{w}) strategy such as proposed by Fraser at al. (1973) and Barcilon et al. (1979). In a saturated environment the linear wave equations can be written into exactly the same form as in a dry environment if the Brunt–Vaisala frequency in the dry wave equations is replaced by an equivalent wet buoyancy frequency, N_{w} (Lalas and Einaudi, 1974; Fraser et al., 1973; Durran and Klemp, 1982b). Therefore, in principle, if N_{w} is known a priori, dry flow dynamics can be directly applied to moist processes without explicitly solving for latent heating/cooling rates. Unfortunately, the cloud boundary, i.e. the saturated region, is usually not known a priori. Therefore, one has to specify the cloud boundary, otherwise a complicated iteration is required to find the cloud boundary as well as N_{w} distribution (Barcilon et al., 1979; Barcilon and Fitzjarrald, 1985). Nevertheless, the moist N (i.e., N_{w}) concept was still widely used to interpret moist effect in case studies (Katzfey, 1995). (iii) Numerical simulations with simple cloud physics such as those considered by Durran and Klemp (1982a; 1983). In these papers, Durran and Klemp addressed issues such as moist mountain lee wave and moist mountain drag with a mesoscale model. For example, Durran and Klemp (1983) applied a two-dimensional convective cloud model to the simulation of the 11 January 1972 severe downslope windstorm over Boulder, Colorado. The addition of moisture decreased the downslope windspeed from 45 to 25 m s^{-1}, due to the weakening of mountain wave amplitude. While their model included full nonlinear dynamics, the cloud physics was highly simplified. Saturated water vapor was instantly condensed, and no other phase change occurred. They demonstrated nicely how the moist effect can modify lee waves and the drag by changing the effective Brunt–Vaisala frequency (i.e., N_w). (iv) Case studies with sophisticated numerical modeling such as Ferretti et al. (2000) and Rotunno and Ferretti (2001). The effect of latent heat release on orographic flow and precipitation has been examined in a number of case studies. For example, Rotunno and Ferretti (2001) suggested that the moisture gradient over the southern side of the Alps played a significant role in the enhancement of precipitation during the Piedmont flood of 4–6 November 1994 as moist southerly airflow impinged on the Alps.

3. Numerical setup

A mesoscale model, Advanced Regional Prediction System (ARPS), is used for this study. ARPS is a nonhydrostatic mesoscale model developed at the Center for Analysis and Prediction of Storms (CAPS) in the University of Oklahoma. The compressible Navier–Stokes equations are solved on a finite grid. For this study, the 1.5 order TKE (turbulence model) and Lin's cloud physics (Lin et al., 1983) are used. Other physical processes such as the radiation model and the soil model are not included for the sake of simplicity.

The model setup can be described as follows. An isolated Gaussian-shaped circular mountain is located in the middle of a square domain. The Gaussian mountain is defined by the following equation

$$h(x, y) = h_m e^{-(x^2+y^2)/a^2} \qquad (1)$$

where h_m is the height of the mountain peak and a is the mountain half-width. The horizontal resolution is $0.2a$. The domain size is $20a$ by $20a$. There are 33 levels in the vertical direction. The vertical coordinate is terrain following, and the resolution is a cubic function of the altitude (Xue et al., 1995). The mountain half-width is $a = 10$ km, and the resulted mountain Rossby number ($Ro = U/fa$) is around 10 for mid-latitude (i.e., $f \sim 10^{-4}$ s^{-1}). Considering that the effect of the earth's rotation should be insignificant, the Coriolis force is set to zero for simplicity. The free advection boundary condition is applied to all four lateral boundaries. Rayleigh damping is applied to the upper boundary to absorb gravity waves. Extensive tests have been performed to examine the sensitivity of solutions to boundary conditions and resolutions. Generally, the results included in this study are robust.

The flow field is initialized using a pseudo-sounding derived analytically from the following parameters: a constant surface air temperature (T_0), a constant buoyancy frequency (N_0), a uniform wind (U_0) and a constant relative humidity (RH). While a range of parameters have been examined, simulations presented in this paper include the following parameters: $T_0 = 270$ K, $RH = 95\%$, $N_0 = 0.011, 0.015$ s^{-1} and $U_0 = 10, 15$ m s^{-1}. Such a combination has a number of advantages. The cold surface temperature is chosen to avoid complexity associated with windward melting (Marwirtz, 1980). The choice of near-saturated air allows us to estimate the moist stability and to use the slab model in its simple form. The windward subcloud evaporation (Carbone et al., 1995) is avoided as well. The resulted moist N is always greater than zero (Jiang, 2000). The limitations of this study associated with the choices of parameters will be further discussed in section 6.

The buoyancy in a saturated environment can be expressed as (Cotton and Anthes, 1989)

$$B = g\frac{\theta'}{\overline{\theta}(z)} + 0.61gq_v' - gq_l \qquad (2)$$

where B is buoyancy force per unit mass, g is the acceleration due to gravity, θ' is potential temperature perturbation, $\overline{\theta}(z)$ is potential temperature of the base state, q_v' is perturbation of water wave mixing ratio, and q_l is liquid water. Based on the sounding information, one can estimate the contribution from each term. For example, if a parcel of one cubic metre is lifted 1 km from the ground ($P_0 = 1000$ mbar), it condenses roughly 0.6 g of water vapor. The corresponding contribution to B from condensation is about 0.044 m s^{-2}, from water loading is about 0.004 m s^{-2}, and from virtual temperature effect is even smaller. It is quite clear, for the chosen parameter, virtual temperature and water loading effects are less important.

The simulations are integrated to a 5-h time. For example, some fields for a vertical section along the center streamline of a simulation with $N = 0.011$ s^{-1}, $U_0 = 10$ m s^{-1}, and $h_m = 1000$ m are plotted in Fig 1. One can see that flow is decelerated over the windward slope (Fig. 1a) associated with ascent (Fig. 1b), and accelerated over the lee-slope associated with strong downdraft (Fig. 1b). However, the strongest deceleration and updraft occur aloft over the lee slope due to the steepening of propagating waves (Fig. 1c). With moisture, clouds can form over the windward slope of the mountain due to stable ascent and over the lee side due to gravity wave lifting (Figs. 1d–1f).

4. Moist effect on dynamics

4.1. *Moist flow stagnation*

The nondimensional mountain height M (or mountain Froude number $Fr = 1/M$) was widely used in

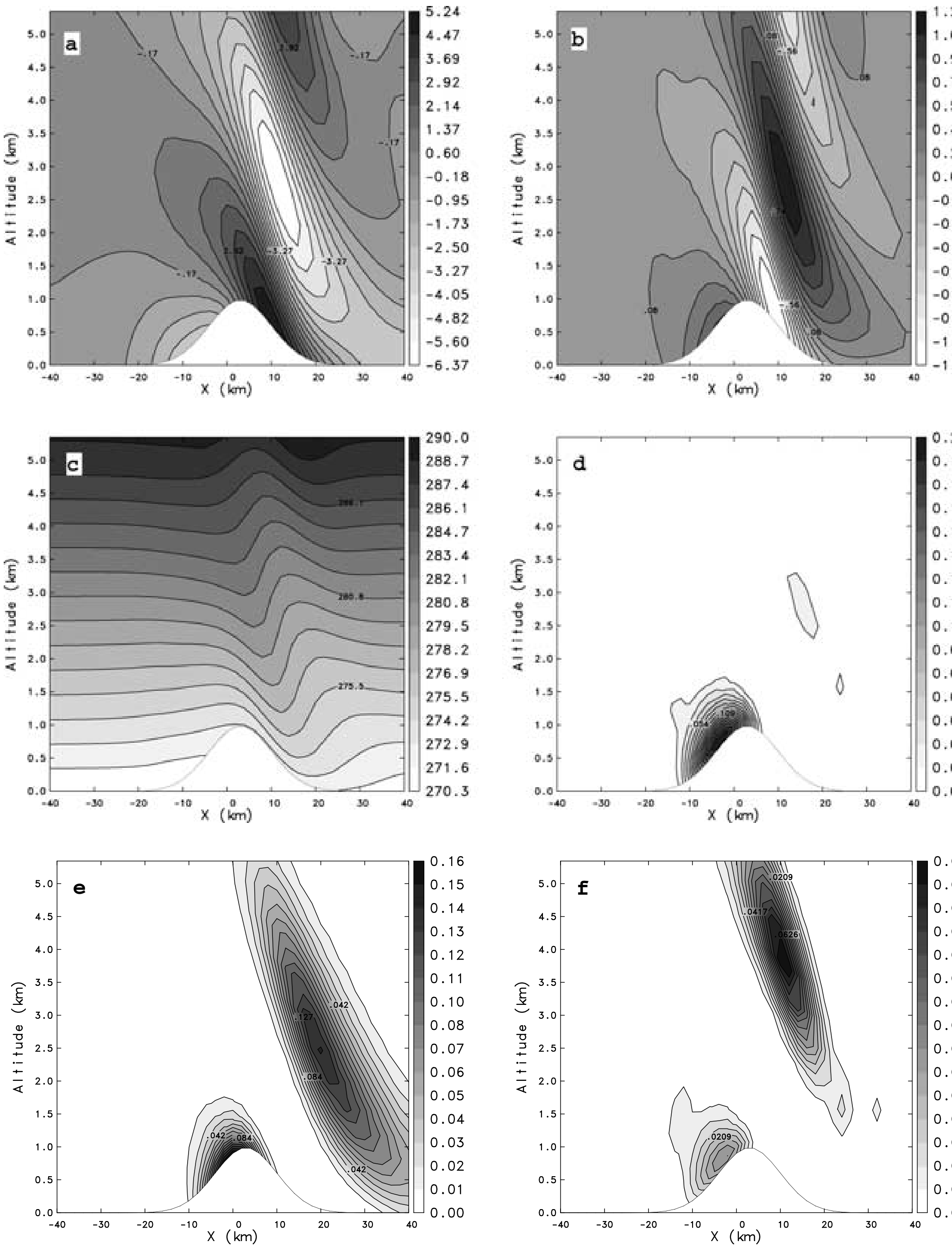

Fig. 1. Vertical cross-section of the steady-state solutions through the domain center simulated by ARPS model. The control parameters are $N_{\mathrm{d}} = 0.011\ \mathrm{s}^{-1}$, $U_0 = 10\ \mathrm{m\ s}^{-1}$, $T_0 = 270$ K, $RH = 95\%$, $a = 10$ km, and $h_{\mathrm{m}} = 1000$ m. Only a portion of the domain is plotted. (a) Stream-wise (u) component of perturbation velocity (m s^{-1}); (b) vertical velocity (w, m s^{-1}); (c) potential temperature (K); (d) mixing ratio of cloud water (g kg^{-1}); (e) mixing ratio of snow (g kg^{-1}); (f) mixing ratio of cloud ice (g kg^{-1}).

the study of stratified flow over terrain. In the hydrostatic limit, M is the only control parameter in the linearized system that governs uniformly stratified inviscid Boussinesq fluids (Smith, 1989). The validity of using M to describe nonlinear features of mountain flow was verified by Smith and Grønås (1993). They demonstrated that curves of nondimensional wind minima over the lee slope (i.e., u_{A}/U_0) and windward slope (i.e., u_{B}/U_0) versus M collapse onto two universal curves, which indicates that flow deceleration is uniquely controlled by the single parameter, M.

For comparison, flow deceleration curves created by Smith and Grønås (1993) are reproduced based on 10 ARPS runs carried to steady state with dry incoming flow (solid curves in Figs. 2a and 2b). The critical mountain height for lee-side flow stagnation aloft (stagnation point A) is about 1.1, which agrees well with Smith and Grønås (i.e., 1.1 ± 0.1). The critical mountain height for windward stagnation (stagnation point B) is around $M_{Bc} = 1.32$, which is smaller than Smith and Grønås (i.e., 1.6). However, their M_{Bc} for flow splitting was derived by extrapolation, because once gravity wave-breaking (GWB) occurred, their solutions started to evolve in time, and no steady state could be achieved.

To illustrate the effect of moisture on flow deceleration and stagnation, four groups of moist runs are shown in Figs. 2a and 2b, and the control parameters are listed in Table 1. It seems that the addition of moisture weakens the mountain induced gravity wave steepening, and delays the onset of wave breaking (Fig. 2a). This moisture modification effect appears to be insensitive to the mountain width and wind speed. For the given parameters, the critical mountain height for the onset of GWB is $M_{Ac} = 1.4 \pm 0.1$, which is almost 30% higher than the corresponding dry case. Moist flow stagnation on the lee side shows modest sensitivity to the buoyancy frequency N_d.

The addition of moisture also causes a strong delay of windward stagnation (Fig. 2b). With $N_{\mathrm{d}} = 0.015$ s^{-1}, the critical mountain height for windward flow splitting (M_{Bc}) is 1.7, which is about 30% larger than the corresponding dry case. For $N_{\mathrm{d}} = 0.011$ s^{-1}, $M_{Bc} \sim 3.0$, which is more than twice the critical height of the corresponding dry case. Again, windward flow deceleration shows weak dependence on both wind speed and mountain width.

From Fig. 2b, the variation of u_{B}/U_0 with nondimensional mountain height is not uniform for both dry and wet cases. Each of those curves can almost be separated into two segments: for low mountain heights, u_{B}/U_0 decreases slowly and linearly with increasing mountain height; near the critical mountain height, u_{B}/U_0 drops to zero sharply, probably due to strong nonlinearity near stagnation points. This observation suggests that the critical mountain height may have

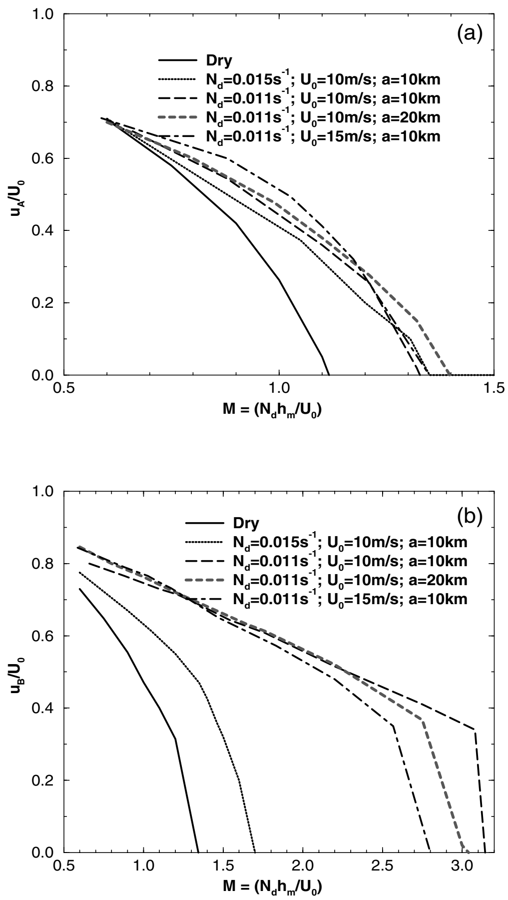

Fig. 2. (a) Plots of flow deceleration curves derived from numerical runs to steady states. u_{A}/U_0 versus M. (b) Plots of flow deceleration curves derived from numerical runs to steady states (u_{B}/U_0 versus M). Five groups of runs are plotted. The control parameters are listed in Table 1.

Table 1. *Control parameters*

Group	U_0 (m s^{-1})	N_{d} (s^{-1})	a (km)
1	10	0.011	10
2	15	0.011	10
3	10	0.011	20
4	10	0.015	10

been overestimated in Smith and Grønås (1993) by extrapolation. It also implies that the transition from the flow-over to flow-around regime can be sudden.

4.2. Moist N_w approach

Previous studies suggested that moist flow dynamics can be understood by using an equivalent N_w to replace the N_d in dry dynamics (Fraser et al., 1973; Barcilon et al., 1979; Durran and Klemp, 1982b). The question is whether we can find an appropriate moist N (i.e., N_w) to rescale M that allows curves shown in Figs. 2a and 2b to collapse onto their corresponding dry curves.

Ignoring the falling of hydrometers and ice-related processes, the equivalent N_w can be written as (Lalas and Einaudi, 1974; Durran and Klemp, 1982b)

$$N_\mathrm{w}^2 = \frac{g}{T}\left(\frac{\mathrm{d}T}{\mathrm{d}z} + \Gamma_\mathrm{m}\right)\left(1 + \frac{Lq_\mathrm{v}}{RT}\right) - \frac{g}{1+q_\mathrm{w}}\frac{\mathrm{d}q_\mathrm{w}}{\mathrm{d}z} \tag{3}$$

where $q_\mathrm{w} = q_\mathrm{v} + q_\mathrm{c}$ is the total water mixing ratio, and q_v and q_c are mixing ratios of water vapor and cloud water, respectively. L is the latent heat of evaporation and R is the ideal gas constant for dry air. Γ_m is the moist adiabatic lapse rate, which is given by

$$\Gamma_\mathrm{m} = \Gamma_\mathrm{d}(1+q_\mathrm{w})\left(1 + \frac{Lq_\mathrm{v}}{RT}\right) \times \left\{1 + \frac{c_{p\mathrm{v}}q_\mathrm{v} + c_\mathrm{w}q_\mathrm{l}}{c_p} + \frac{\epsilon L^2 q_\mathrm{v}}{c_p R T^2}\left(1 + \frac{q_\mathrm{v}}{\epsilon}\right)\right\}^{-1} \tag{4}$$

where c_p, $c_{p\mathrm{v}}$ and c_w are heat capacities of dry air, water vapor and liquid water under a constant pressure, and $\epsilon = 0.622$ is the ratio of the gas constants for dry air and water vapor.

The equivalent N_w can be computed from model output based on eq. (3). As an example, for $N_\mathrm{d} = 0.011\ \mathrm{s}^{-1}$, $U_0 = 10\ \mathrm{m\,s}^{-1}$ and $h_\mathrm{m} = 800$ m, N_w is contoured for the vertical section through the centerline (Fig. 3a). Through most of the domain, air is unsaturated, and therefore $N_\mathrm{w} = N_\mathrm{d}$. N_w is strongly reduced only in clouds and the minimum ($0.0031\ \mathrm{s}^{-1}$) is located over the windward slope. The decrease of N_w over the windward slope is caused by both moist processes and vertical stretching of low level flow associated with blocking. Another region with reduced N_w is located in the lee, which is caused by gravity wave induced condensation, snow precipitation and stretching of the low level flow. The moist N derived from modeling is only useful for diagnosis. For prediction or scaling, one has to estimate the moist N from the background flow. Such a "background" moist $N(N_\mathrm{w0})$ can be estimated using eq. (3) by assuming that flow is saturated but with $q_\mathrm{l} = 0$. For a set of N_d, their corresponding N_w0 are plotted in Fig. 3b. In general N_w0 increases with altitude and approaches its corresponding N_d aloft. N_w0 is sensitive to the surface temperature T_0 and the dry stability N_d. For $N_\mathrm{d} = 0.011\ \mathrm{s}^{-1}$ and $T_0 = 270$ K, $N_\mathrm{w0} = 0.004\ \mathrm{s}^{-1}$ at the ground and $0.008\ \mathrm{s}^{-1}$ at about 2.5 km. This strong spatial variability of N_w0 poses an interesting question: how should the most representative N_w be chosen for rescaling?

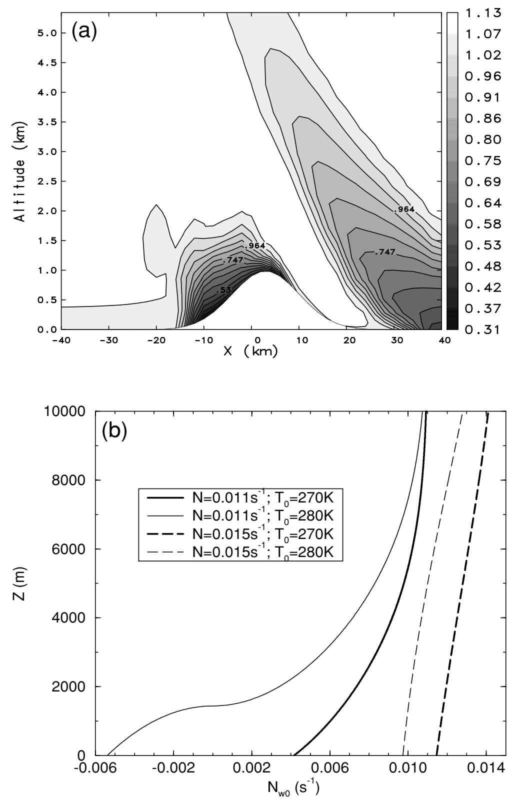

Fig. 3. (a) Vertical section cutting through the center streamline. $100N_\mathrm{w}$ (s^{-1}) is contoured and shaded. N_w is computed from ARPS run using eq. (3) with $q_\mathrm{w} = q_\mathrm{v} + q_\mathrm{c} + q_\mathrm{i} + q_\mathrm{s}$ and $q_\mathrm{l} = q_\mathrm{c} + q_\mathrm{i} + q_\mathrm{s}$, where q_i and q_s is the mixing ratio of cloud ice and snow, respectively. Only a portion of the domain is plotted. (b) Plot of N_w0 versus altitude (z). N_w0 is computed from environment flow based on eq. (3). Four curves are plotted with $N_\mathrm{d} = 0.011, 0.015\ \mathrm{s}^{-1}$ and $T_0 = 270$, 280 K.

A particular rescaling is shown in Fig. 4. For the two groups of runs shown in Figs. 2a and 2b, the flow

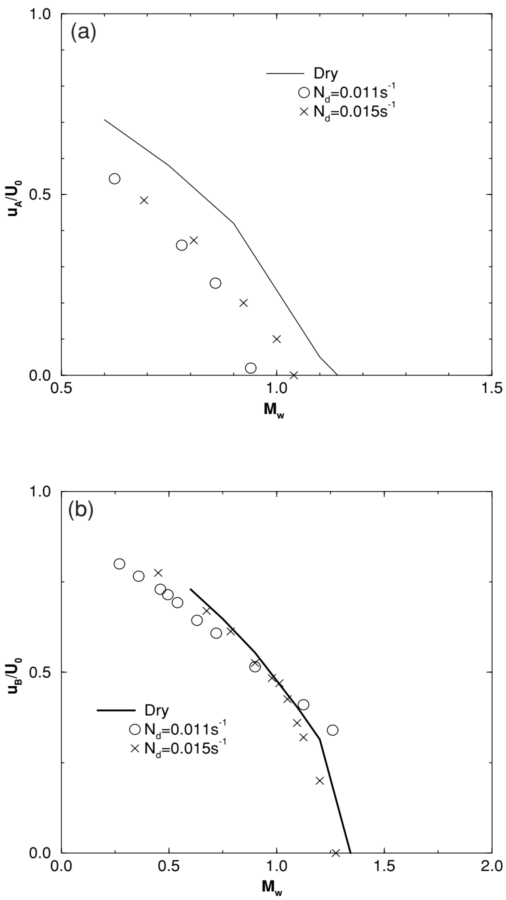

Fig. 4. (a) Plot of u_A/U_0 versus $M_w = N_w h_m/U_0$, where N_w is averaged over the lowest 1 km. A set of dry runs (solid curve) and two sets of moist runs (symbols) are plotted. (b) Plot of u_B/U_0 versus $M_w = N_w h_m/U_0$, where N_w is averaged over the lowest 3 km. A set of dry runs (solid curve) and two sets of moist runs (symbols) are plotted.

deceleration curve B is rescaled using N_{w0} averaged over the lowest kilometre, and the flow deceleration curve A is rescaled using N_{w0} averaged over the lowest 3 km. It appears that the rescaling of curve B is satisfactory. Three widely separated curves shown in Fig. 2b approximately collapse onto one "universal" curve. The finding of universal curve B implies that, despite the complex cloud physics and thermodynamics, windward flow deceleration and stagnation may still be predictable, if the corresponding N_w can be properly estimated from the background flow.

The rescaling of curve A is not as successful (Fig. 4a). The moist effect is exaggerated by the present scaling. The critical moist nondimensional mountain height M_{wc} is 1.0 ± 0.1. If the same moist N for curve B is used, M_{wc} is around 0.7. The different results of rescaling curves A and B suggest that it might be impossible to define a moist nondimensional mountain height to describe the general nonlinearity of mountain flow.

4.3. The effect of precipitation

Precipitation may influence flow dynamics in a number of ways. For example, it may change the distribution of water loading and reduce latent cooling due to evaporation or sublimation. Both effects are ignored in the above N_w argument. As an example, for $U_0 = 10$ m s^{-1}, $a = 10$ km, $N_d = 0.011$ s^{-1} and $h_m = 1000$ m, the latent heating/cooling rate along the vertical cross section through the domain center is shown in Fig. 5. The latent heating/cooling rate is computed from model variables near the end of the simulation. There are two heating/cooling pairs; one near the ground and the other aloft over the lee slope.

In order to isolate the precipitation effect, two special models are constructed, namely a no precipitation model (NP) and a perfect precipitation model (PP). The NP model keeps all the cloud physics described in section 3.1 except that the terminal velocity of hydrometeors is set to zero. Therefore, there is no precipitation in the NP runs and all the water species are

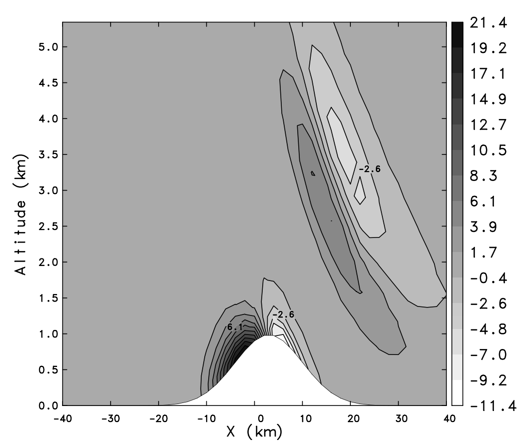

Fig. 5. The vertical cross-section through the domain center. The local latent heating/cooling rate (Watts) is contoured/shaded based on the ARPS run with $U_0 = 10$ m s^{-1}, $N_d = 0.011$ s^{-1} and $a = 10$ km. The latent heat release due to the moist processes is averaged over the last 20 timesteps (i.e., 200 s). Only a portion of the domain is plotted.

Table 2. *The effect of precipitation on dynamics*

Model	u_A/U_0	u_B/U_0	u_{max}/U_0	Drag (N)
NP	0.383	0.727	1.51	5.67×10^8
ARPS	0.348	0.732	1.53	6.15×10^8
PP	0.40	0.81	1.53	6.37×10^8

carried over to the lee side, where they sublimate or evaporate. All condensed water falls to the ground instantly in the PP model. There is no sublimation and evaporation; therefore, there is no latent cooling over the lee slopes in the PP runs. PP model will be further discussed in section 5. For $N = 0.011$ s^{-1}, $U = 10$ m s^{-1}, $h_m = 1000$ m, $T_0 = 270$ K and $RH = 0.95$, results from three different models, NP, ARPS and PP, are shown in Table 2.

Another common index to describe the dynamical influence of mountains on the atmosphere is mountain drag, $D = \int_{-\infty}^{\infty}\int_{-\infty}^{\infty} P' h_x \, dx \, dy$ (Smith, 1979), where P' is surface pressure perturbation. From Table 2, precipitation seems to change mountain drag slightly. Compared to the NP run, the mountain drag is increased by 11% in the PP run. Precipitation weakens windward flow deceleration. Therefore, it helps to delay the onset of flow splitting, but the overall change is small. From Table 2, the role of precipitation in lee-side wave steepening is not clear. Both NP and PP runs show an increase in u_A/U_0.

Overall, the effect of precipitation on dynamics is small over the range of parameters examined. This finding provides an extraordinary simplification to the subject of orographic precipitation, reducing the effect of microphysics on dynamics. However, readers should be reminded of the limitations of this result associated with the choice of base states. For example, sub-cloud evaporation/melting (which may change sub-cloud stability) is avoided in the model by choosing the near-saturated incoming airflow.

5. Dynamics and precipitation

One of the major factors that controls orographic precipitation is the forced ascent, which determines how much water vapor becomes saturated. As found in previous case studies, terrain lift effect can be strikingly different for different flow regimes (i.e., flow over or flow around). The focus of this section is the effects of mountain flow dynamics on the intensity and distribution of precipitation.

5.1. Precipitation models

Five precipitation models of varying complexity are used. The physics and dynamics included in each model are described below.

ARPS: As described in section 3, the ARPS model is a nonhydrostatic model with full dynamics and cloud physics. For this study, Lin's cloud parameterization (Lin et al., 1983) is used. There are six water species: water vapor, cloud water, cloud ice, rain water, snow and hail. Water vapor, cloud water and cloud ice are carried with air. Rain water, snow and hail fall at some finite terminal speed. Given that the ground temperature is below freezing point in this study, little rain water is generated. Hail generation is insignificant as well, considering that no convection occurs. Therefore, the only precipitable hydrometeor is snow. More detailed description and diagnosis of Lin's scheme can be found in Lin et al. (1983) and Jiang and Smith (2003).

Perfect precipitation model: An extreme situation occurs when hydrometeors grow and fallout so fast that all the condensed water falls immediately to the ground. Because the precipitation efficiency is always 100%, this model is referred to as the "Perfect precipitation" (PP) model. In this study, the perfect precipitation model is created by modifying the ARPS model so that all the saturated water vapor falls to the ground instantly. The only moist process in such a model is saturation adjustment. The saturation mixing ratio is calculated using Teten's formula (Xue et al., 1995). While the PP model retains full dynamics and thermodynamics, ice-phase cloud physics, hydrometeor drift, evaporation and sublimation are not taken into account. A comparison between the PP model and the full ARPS model helps to isolate the effect of cloud parameterization in orographic precipitation.

No-latent-heat model: To isolate the role of latent heat release in orographic precipitation and associated lee side drying, a "No-latent-heat" (NLH) model is constructed by turning off all latent heat release in the ARPS model. This is accomplished by setting the latent heat of vaporization $L = 0$ in the thermodynamical equation.

No-latent-heat perfect precipitation model: A "No-latent-heat perfect precipitation" (NLH_PP) model is constructed by setting $L = 0$ in the PP model.

Slab model: Over the last couple of decades, simple slab models have become more and more popular in the studies of orographic precipitation, especially when applied to hydrology (e.g. Colton, 1976;

Rhea, 1978), regional climate (e.g. Sinclair, 1994) and glaciology (e.g. Sanberg and Oerlemans, 1983). Slab models are computationally cheap, and their predictions are easy to interpret. Although only simple dynamics and physics are included, these models were found surprisingly successful, particularly in the statistical sense (e.g. Sinclair, 1994).

A prototype model of upslope precipitation was derived by Smith (1979). Precipitation rate over the windward slope can be estimated analytically based on the following assumptions: the incoming flow is saturated and moistly neutral; a fixed fraction (ϵ) of the condensed water falls to the ground instantly; streamlines are parallel to the ground surface at all levels. If the incoming flow is unsheared $\vec{V}(z) = \vec{V}_0$, the local precipitation rate over windward slope (R) is given by

$$R = \epsilon \rho_a q_0 \vec{V}_0 \cdot \nabla h \tag{5}$$

where ρ_a and q_0 are the air density and water vapor mixing ratio at the ground, respectively, ∇h is local terrain slope, and ϵ is the constant precipitation efficiency. Hereafter, we refer to a slab model with a specified precipitation efficiency ϵ as a slab_ϵ model. For example, slab_20 means PE = 20%.

For this study, the incoming airflow is unidirectional ($\vec{V}_0 = U_0 \vec{i}$) and the terrain is Gaussian shaped [eq. (1)], we obtain

$$R = -2\epsilon \rho_a q_0 U_0 \frac{x}{a^2} h(x, y). \tag{6}$$

Equation (6) suggests that the precipitation rate is proportional to the windspeed U_0, moisture content q_0 and the mountain height h_m.

5.2. *Precipitation intensity and mountain height*

The precipitation rate maxima derived from the four groups of moist runs listed in Table 1 are plotted in Fig. 6 with corresponding slab_20 model predictions.

For a given mountain height, the maximum precipitation rate ($P_{\max}$) seems to increase with windspeed and decrease with increasing mountain half-width, as suggested by the slab model (6). Dynamically, the increase of wind speed will enhance the mountain lifting effect and therefore generate more condensation and precipitation. The increase of mountain width makes the local mountain slope more gentle and reduces the vertical motion. Therefore, the precipitation is weaker accordingly. Figure 6 also indicates that the more stable the incoming air, the weaker the precipitation. While the stability effect is not included in the simple slab model, this observation is consistent with our understanding that generally stability tends to restrain vertical motion.

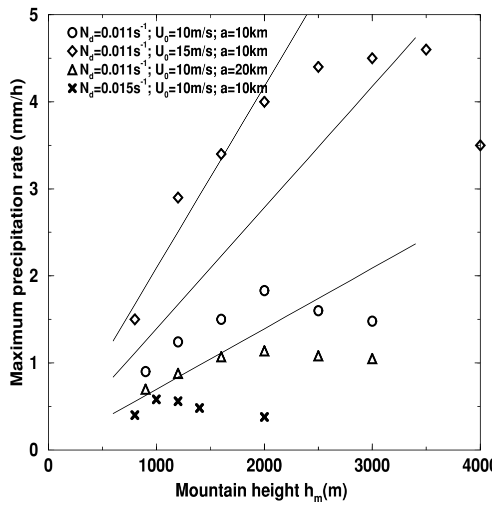

Fig. 6. Plot of the maximum precipitation rate versus mountain height. Symbols are for ARPS simulations. Four groups of runs are plotted. The control parameters are listed in the legend. The thin solid lines are predictions of the slab model for corresponding runs.

Over a certain range of mountain heights, all four groups of runs show an increase of precipitation with mountain height (Fig. 6). The slopes of the curves show reasonable agreement with the slab_20 model, which implies that the maximum precipitation rates are linearly dependent on the mountain height. The linear dependence on mountain height eventually breaks down as the mountain becomes too high. Beyond certain critical mountain heights (denoted as h_{pc}), the local precipitation rates no longer increase with mountain height or even begin to decrease. The critical mountain heights appear to be related to the moist nondimensional mountain heights. Approximately, for Groups 1 and 3, $h_{pc} = 2000$ m, for Group 2, $h_{pc} = 3500$ m, and for Group 4, $h_{pc} = 1000$ m. The corresponding nondimensional heights $M_{pc} = 2.2$, 2.56 and 1.5 and the corresponding moist nondimensional heights $M_{wpc} =$ 1.2, 1.4 and 1.1. The difference in the critical M_{wpc} for the four groups of runs might be due to microphysics.

A plausible explanation is that as the mountain becomes too high, more low-level moist air passes around the peak, which reduces the mountain lifting effect. Therefore, the condensation and precipitation due to mountain lifting are reduced correspondingly.

This issue is further examined in the remainder of this section. In the discussion above, the precipitation efficiency (PE) is assumed to be 20%. The variation of PE and its impact on the conclusions will be discussed in section 5.5.

5.3. Blocking effects and precipitation

To examine the effect of flow splitting on the intensity and distribution of precipitation, three sets of simulations are carried out using all five models. The base state is given by $N_d = 0.011\ s^{-1}$, $U_0 = 10\ m\ s^{-1}$, $T_0 = 270$ k and $RH = 95\%$. The three sets of runs correspond to flow-over ($h_m = 800$ m, $M = 0.88$ and $M_w = 0.48$), marginal ($h_m = 2000$ m, $M = 2.2$ and $M_w = 1.2$), and flow-around ($h_m = 3000$ m, $M = 3.3$ and $M_w = 1.8$), respectively.

For the flow-over situation, the slab_100 model (Fig. 7a) indicates that precipitation occurs over the windward slope, and the maximum is located about 7 km upstream of the peak where the slope is the steepest. The width of the precipitation area is roughly equal to the mountain width. The PP model predicts two separate precipitation patches, the windward patch related

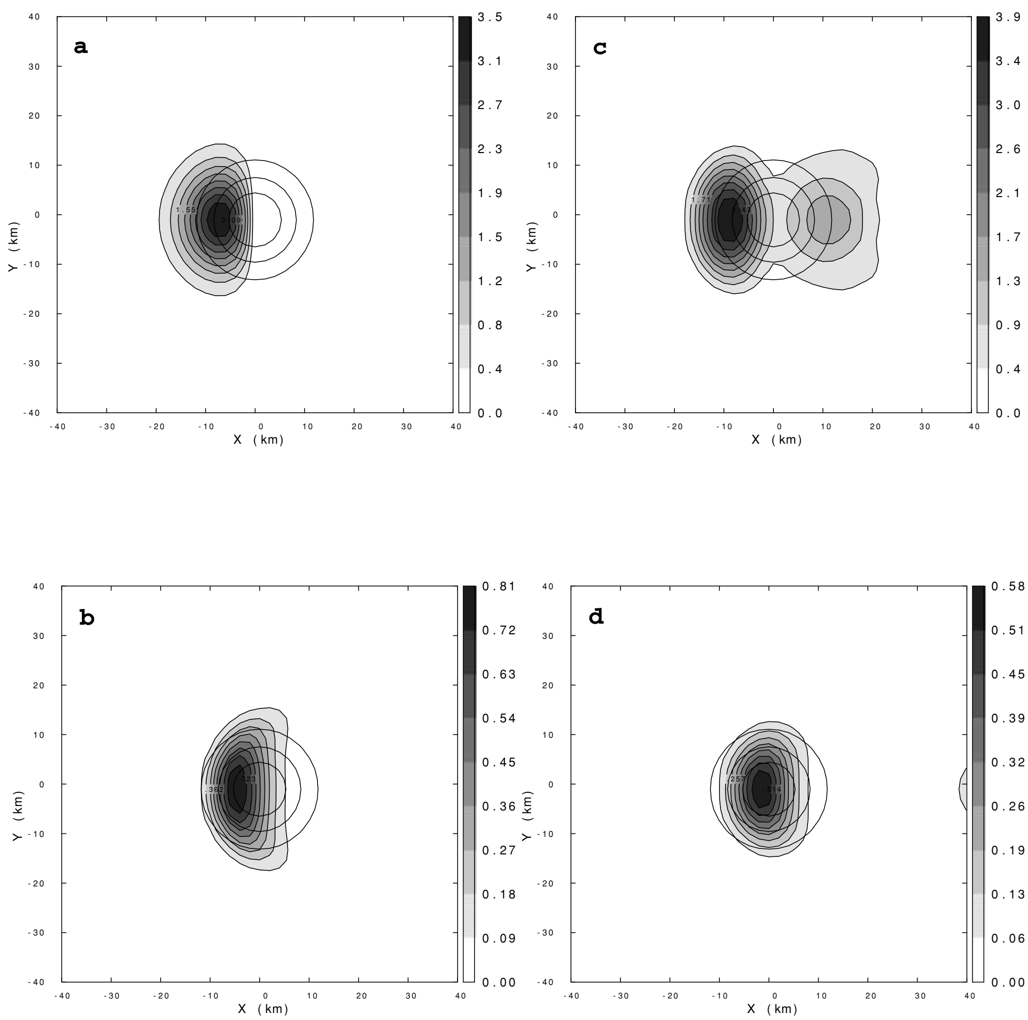

Fig. 7. Precipitation rates (mm h^{-1}) for a flow-over case ($N_d = 0.011\ s^{-1}$, $U = 10\ m\ s^{-1}$, $h_m = 800$ m, $T_0 = 270$ K and $RH = 95\%$). (a) Slab model, (b) NLH model, (c) PP model and (d) ARPS model.

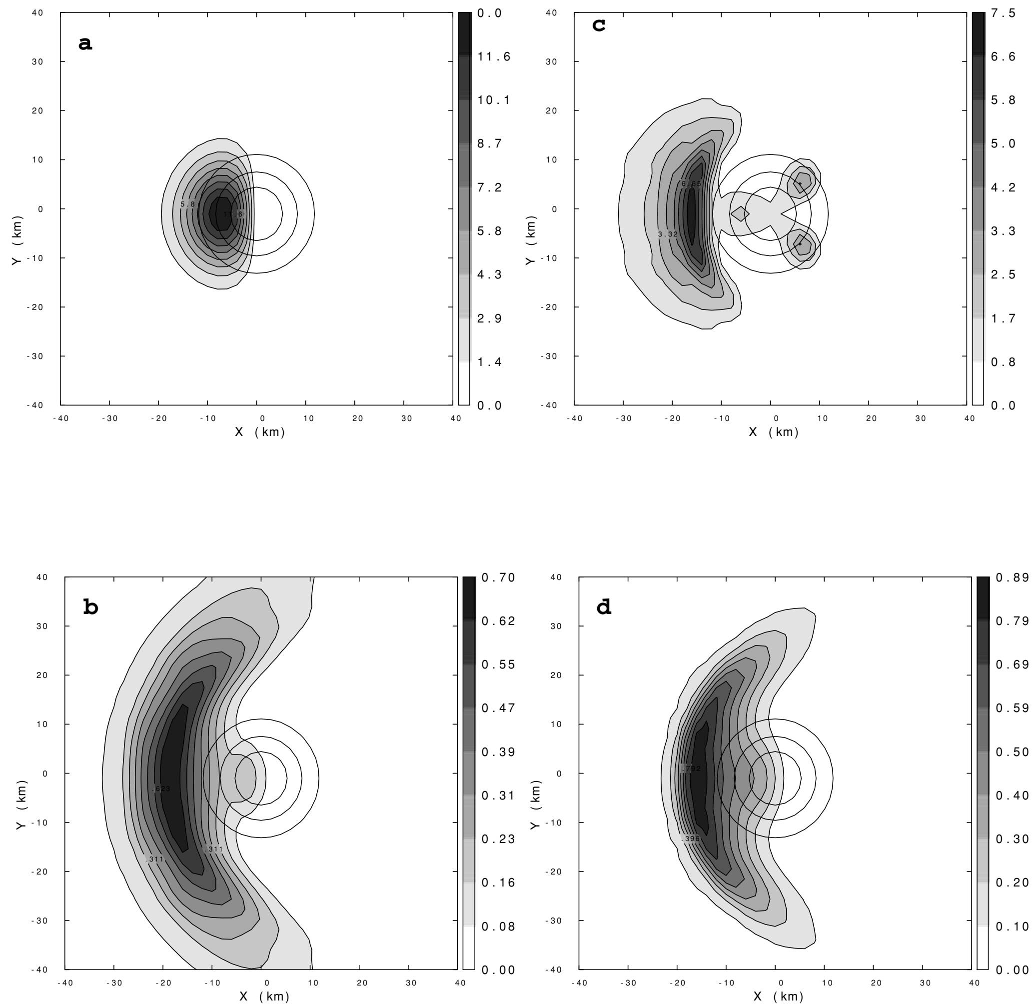

Fig. 8. Same as Fig. 7 except for $h_{\mathrm{m}} = 3000$ m.

to upslope ascent, and the lee-side patch induced by gravity wave aloft (Fig. 1). The maximum precipitation rate from the PP model is about 10% larger. The dimensions and shapes are quite similar. The location of the precipitation maximum is about 9 km upstream of the peak according to the PP model. The upstream shift should be associated with the nonlinear blocking effect, which is not included in the slab_100 model. The other two models with cloud physics predict similar precipitation patterns with much reduced precipitation rates. Most condensate is carried over to the lee side and evaporated. The precipitation maximum is located about 3 km upstream of the peak according to the ARPS model, and some spill-over (i.e., precipitation over the lee-side) can be seen. The location of the precipitation maximum is about 5 km upstream of the peak according to the NLH model.

For the flow-around case, the precipitation pattern and its location predicted by the slab_100 are identical to the flow-over case, but the precipitation rate is higher (Fig. 8a). The corresponding PP model prediction is quite different (Fig. 8c). There are three precipitation patches: the lee-side patch, the windward slope patch and the arc-shaped precipitation band detached from the terrain. The maximum precipitation rate reaches 7 mm h $^{-1}$, and is located about 15 km upstream of the peak, where the terrain is much gentler. Similarly, the two models with cloud physics (Figs. 8b and 8d) predict a detached precipitation band and a "tail" over the windward slope with much weaker precipitation. Compared to the corresponding PP run, the precipitation rates predicted by the NLH and the ARPS models are much weaker due to low precipitation efficiency. It is interesting that for the flow-around case, little spill-over is observed (Figs. 8b and 8d).

For the PP, NLH and ARPS models, the precipitation maxima are located about 10–20 km upstream of the peak, where the terrain slope is insignificant and the associated upslope ascent should be small. The reason can be clearly seen in Fig. 9. For the flow-over case the vertical motion reaches a maximum over the windward slope (Fig. 9a), where the precipitation maximum is located according to Fig. 7d. For the flow-around case, the field is much more complex. First, there is a broad area with weak descent over the terrain. Over the windward slope, the descent is caused by low-level flow reversal associated with the formation of stagnation points. Over the flanks, the descent is induced by the deflection of incoming flow. Near the peak, there is a small area over the windward slope with $w > 0$. Along the front of the reversed flow there is an arc-shaped band with small positive w. Further downstream there is a pair of eddies with flow reversal near the center line, as found in a number of studies (e.g., Smolarkiewicz and Rotunno, 1989; 1990). Nevertheless, Fig. 9b suggests that we can not relate the arc-shaped precipitation pattern found in Figs. 8b–8d to direct mountain lifting. From Fig. 10a we can see clearly that the maximum of the snow mixing ratio is located about 15–18 km upstream of the peak, where the mountain slope is very gentle. The cloud (snow) can be separated into two parts. One part sits about

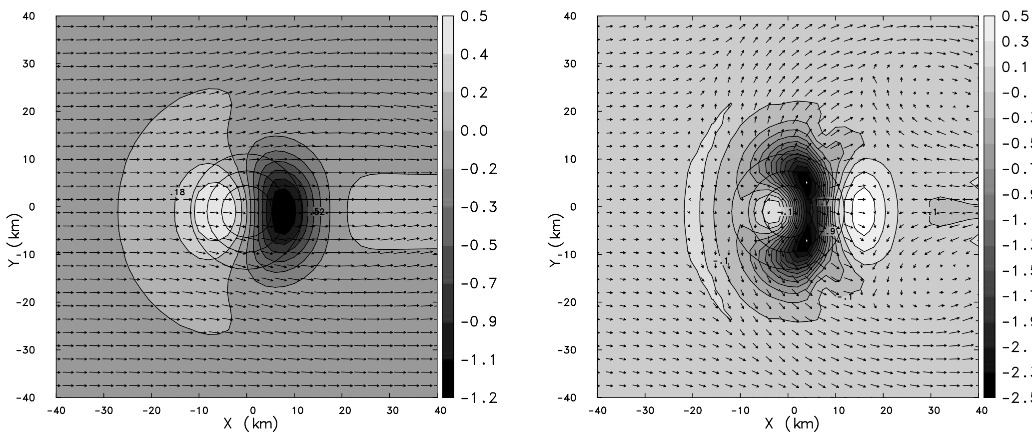

Fig. 9. Wind field (arrows) and vertical motion (in gray scale) at the surface for two runs. (a) Case I, (b) Case II.

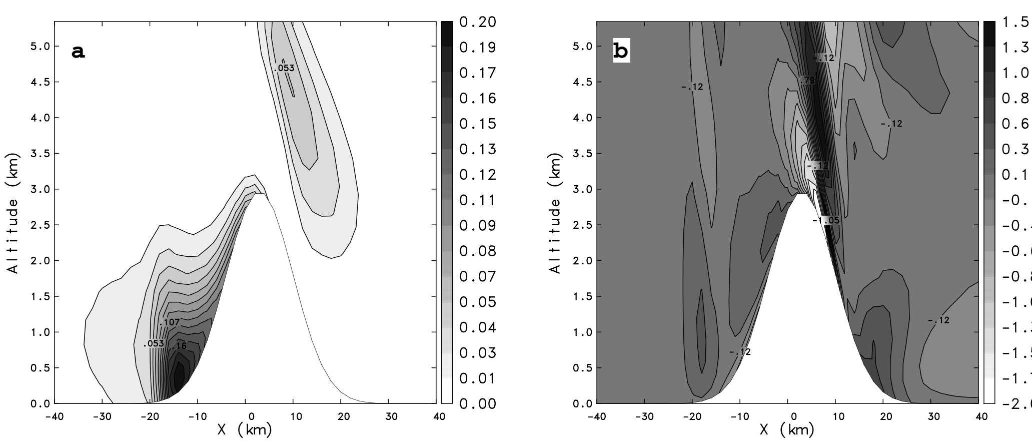

Fig. 10. Vertical cross-section through the domain center. ARPS simulation of the flow-around case is shown. (a) Mixing ratio of snow (g kg^{-1}); (b) vertical velocity (m s^{-1}).

15–18 km upstream of the peak, creating the arc-shaped precipitation band. The other part is located near the peak, associated with direct upslope ascent. This separation is supported by Fig. 10b as well. There are two distinct regions with flow ascent. One region sits at about 18 km upstream of the peak, and is detached from the terrain with maximum updraft approximately 1 km above the ground, the other region over the windward slope and near the peak, with updraft maxima at the surface.

The plausible dynamics for this detached updraft is illustrated in Fig 11. As flow approaches a high mountain, two stagnation points, s_1 and s_2, appear over the windward slope (Hunt and Snyder, 1980; Smolarkiewicz and Rotunno, 1990; Baines and Smith, 1993). Flow is reversed between s_1 and s_2, as we have seen from Fig. 9b. The convergence of the incoming flow and the reversed flow forces air to ascend near point s_1. We refer to this as the dynamically forced secondary circulation. This interpretation is supported by Fig. 9b as well. The upstream boundary of the reversed flow roughly coincides with the arc-shaped precipitation band.

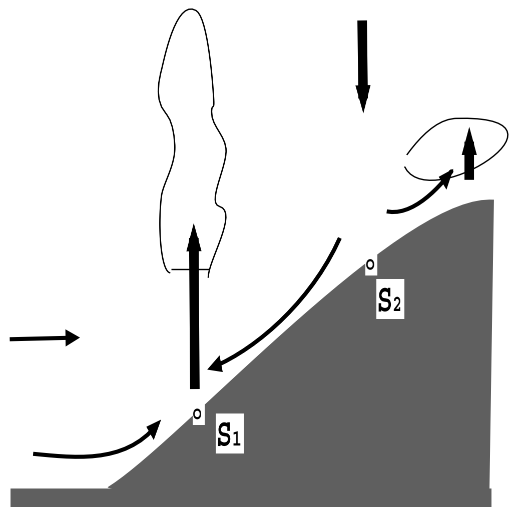

Fig. 11. Sketch of the secondary circulation forced by mountain blocking. There are two stagnation points, S_1 and S_2. The vertical motion is represented by vertical arrows. The upstream flow is from left to right.

5.4. *The effect of latent heat on upslope precipitation*

The importance of latent heat on upslope precipitation has been noticed in a number of studies (e.g., Smith and Lin, 1982; Rotunno and Ferretti, 2001). To examine the interactions between latent heating and blocking and their impact on precipitation, some dynamical and precipitation indices derived from simulations are listed in Table 3. Predictions from two pairs of models are compared: ARPS versus NLH and PP versus NLH_PP. In Table 3, $P_{\max}$ (mm h^{-1}) is the maximum precipitation rate, X_{pmax} (km) is the location of the precipitation maximum, P_{tt} (kg h^{-1}) is the area integrated total precipitation rate, and $C_{\max}$ (s^{-1}) is the maximum horizontal divergence (i.e., $\nabla_H \cdot \vec{v}$) at the surface. Here $C_{\max}$ is used as an index of windward flow blocking. *PE* is defined as the ratio of windward area integrated precipitation rate and the windward volume integrated condensation rate. If we assume that the average precipitation rate is half of $P_{\max}$, the precipitation area is given by $2P_{\mathrm{tt}}/P_{\max}$.

Table 3. *The effect of latent heat: inter-model comparisons*

h_m (m)	Model	$P_{\max}$ (mm h^{-1})	X_{pmax} (km)	P_{tt} (10^8 kg h^{-1})	$C_{\max}$ (10^{-3} s^{-1})	Area (km^2)	PE (%)	$u_{\min}$ (m s^{-1})
800	ARPS	0.61	3	0.62	1.0	200	25	7.7
	PP	4.95	9	4.0	0.75	316	100	7.4
	NLH	0.86	7	0.95	1.7	220	24	5.3
	NLH_PP	3.64	10	6.48	1.7	365	100	5.2
2000	ARPS	1.35	9	2.2	3.8	326	28	4.6
	PP	6.27	13	10.84	3.7	345	100	4.7
	NLH	0.80	15	2.9	3.3	725	29	−1
	NLH_PP	5.9	17	19.7	3.4	667	100	−1
3000	ARPS	0.94	16	3.8	3.9	808	29	−3
	PP	10.4	19	16.72	4.1	322	100	−2
	NLH	0.76	19	6.4	3.9	1684	30	−2
	NLH_PP	3.6	21	26.44	4.3	1469	100	−3

For $h_m = 800$ m, turning off latent heat causes more severe windward blocking (i.e., a smaller u_{min} and a larger C_{max}) and tends to move precipitation patterns upstreamwise (see X_{pmax}), which is consistent with the moist N argument. NLH predicts stronger precipitation than ARPS does in terms of P_{max} and P_{tt}. However, the NLH_PP model predicts a smaller P_{max} and a larger P_{tt} than the PP model does.

For a very high mountain ($h_m = 3000$ m), both the NLH and ARPS models predict a similar arc-shaped precipitation pattern (Figs. 8b and 8d) which extends further downstream around the flanks. The no-latent-heat models (NLH and NLH_PP) predict more widespread but weaker (i.e., smaller P_{max}) precipitation, and the location is further upstream. The role of latent heat in blocking relief is clear.

The marginal case ($h_m = 2000$ m) is most sensitive to latent heating. Turning off latent heat causes a transition from flow-over to flow-around. The precipitation band shifts 4km upstreamwise. The total precipitation is almost doubled (NLH_PP versus PP), but the local maximum rate is reduced (NLH_PP versus PP and NLH versus ARPS).

In summary, no-latent-heat models tend to produce a weaker and widespread precipitation pattern. Generally, latent heat tends to enhance local precipitation maximum as well except for one of the flow-over pairs (ARPS versus NLH). For the flow-over case, ARPS predicts a smaller P_{max} than NLH. However, the fact that PP predicts a larger P_{max} than NLH_PP suggests that the exception might be associated with cloud physics.

5.5. Separating dynamics, thermodynamics and cloud physics

To understand the effect of the dynamics on precipitation, it is important to isolate the microphysical effects. Strictly speaking, however, it is impossible to completely separate the effects of dynamics and cloud physics due to complex interactions among dynamics, thermodynamics and cloud physics.

Here we assume that the differences between the predictions by the ARPS model and the PP model are caused solely by microphysics. Similarly, the differences between the NLH model and the NLH_PP model indicate the effect of cloud physics as well. This assumption allows us to isolate the cloud physics effect by comparing model predictions. From Table 3, the influence of cloud physics on precipitation is significant. The hydrometeors drift can shift the precipitation pattern 4–7 km further downstream. Cloud physics also tends to spread the precipitation and therefore reduces the local precipitation maxima. Models with cloud physics suggests that PE is far less than 100% in this study. For the three cases listed in Table 3, PE varies from 25% to 30% for the ARPS and the NLH model. The influence of latent heat on PE is minor for all three cases. According to Jiang and Smith (2003), PE varies with a number control of parameters. For example, PE can be significantly increased by increasing the mountain width, which increases the advection timescale (i.e., $\tau_a = a/U_0$). A longer advection timescale allows more condensed water to convert to precipitable particles and more snow particles to fall over the windward slope. PE is larger for warmer air, which holds more water vapor, because the increase in the concentration of the condensed water speeds up the nonlinear accretion process and produces more precipitation.

6. Conclusions

The interaction between moist flow stagnation and precipitation is examined based on a limited number of numerical simulations. The effect of latent heat release on flow splitting and gravity wave-breaking demonstrated in this study is quite striking. For example, with RH = 95%, $T_0 = 270$ K and $N_d = 0.011$ s^{-1}, the release of latent heat due to condensation can assist low-level air to ascend over mountains twice the height that dry air can. The delay of flow splitting and gravity wave-breaking can be even stronger if the surface temperature is higher, and more latent heat is released.

In the range of parameters investigated, flow deceleration and stagnation are less sensitive to the mountain width and more sensitive to the stability of the atmosphere. However, it should be pointed out that the rotation of the earth is not taken into account in this study. The modification of flow deceleration and stagnation by moisture and its dependence on control parameters can be qualitatively understood using the moist static stability concept. A nondimensional mountain height is useful for predicting the stagnation point B, which measures windward blocking and flow splitting. However, no satisfactory scaling is found for flow stagnation aloft (point A). One should be cautious in defining a moist nondimensional mountain height ($M = Nh_m/U_0$) as a measure of the general nonlinearity of the system, as in dry mountain flow dynamics. A plausible explanation is that the variation of moist N over one vertical wavelength is too large to give a single characteristic value.

The influence of precipitation on flow deceleration or stagnation seems insignificant according to this study. Although the precipitation changes the evaporative cooling over the lee slope, the signal weakens in both vertical and horizontal directions. Therefore, it has little influence on windward flow field or wave steepening aloft. It should be pointed out that precipitation can be quite important under some special conditions (Marwitz, 1980; Carbone et al., 1995). Using simple slab models to predict orographic-related precipitation is quite popular in areas such as hydrology, regional climate and glaciology because of their low cost in computation and fewer demands of input data. A common feature of these models is that little dynamics and cloud physics are included. This study confirms that slab models can provide a reasonable estimate of the total condensation and the distribution of precipitation if the nondimensional mountain height is small (i.e., $M < 1$). This is so because when M is small, low-level airflow roughly satisfies the assumptions of slab models, i.e., flow over the peak with lift proportional to the terrain slope, and the maximum lift occurs near the steepest slope. As demonstrated, for low mountains, all four models predict similar upslope precipitation patterns. Major differences are caused by cloud physics. The two models with microphysics (NLH and ARPS) predict much weaker precipitation. The precipitation efficiency (the ratio of precipitation rate and condensation rate) derived from NLH and ARPS is less than 30%. Finite falling speed of snow particles in NLH and ARPS models shifts the precipitation pattern downstream.

For high mountains, blocking-induced convergence dominates the windward lift. Especially for very high mountains, blocking may cause flow reversal over the windward slope with a secondary circulation (Fig. 11). The intensity of the detached precipitation band can be much stronger than the precipitation near the peak, which is directly caused by mountain lift. Prediction of precipitation associated with the secondary circulation is beyond the capability of slab models.

A popular argument is that, as a mountain becomes very high, moisture-enriched low-level air can flow around the peak with much reduced lifting, condensation and precipitation. Apparently, this picture is valid only with respect to the condensation and precipitation directly induced by the mountain lift. The missing part of the picture is the secondary circulation forced by blocking and flow reversal, which might cause more intensive precipitation than the direct mountain lift.

The role of latent heat in upslope rain and moisture transport is found to be more complex than in the traditional view. Some previous studies suggested that latent heat effect might enhance precipitation (Rotunno and Ferretti, 2001). This study seems to suggest that while turning-off latent heat tends to reduce the maximum precipitation rate, it also broadens the effective width of the terrain (not a two-dimensional effect) and increases precipitation area over the forward mountain slopes. In other words, it drains more water vapor out of the passing air. The conflict cautions against the generalization of these results. The contribution of latent heat to orographic precipitation might be dependent on a number of factors such as terrain shape, moisture distribution in the air and in-flow stability. Further study is needed to clarify this issue.

Finally, the limitations associated with the choices of base states should be emphasized. Relative to the almost infinite choices one can make for the surface temperature and the vertical distribution of temperature, moisture and wind, the work presented here only covers a small parameter space. For example, near saturated incoming flow is chosen for convenient application of the slab model. Such a choice also excludes some important processes such as sub-cloud melting (Marwitz, 1980) or evaporation (Carbone et al., 1995). To avoid the occurrence of convection, a cold surface temperature is chosen and accordingly the only precipitable hydrometeor is snow in the model. The much slower falling speed of snow (compared to rain drops) reduces precipitation efficiency and shifts the precipitation pattern further downstream (Jiang and Smith, 2003). Nevertheless, $T_0 = 270$ K is a quite typical surface temperature for winter time mid-latitude area.

7. Acknowledgments

The author is grateful to Dr. Ronald B. Smith for illuminating discussions and review of the manuscript. Thanks go to Drs. Brian Colle, James D Doyle, Richard Rotunno, George Veronis and Wendy Welch Orlando for their helpful comments. This research was supported by the National Science Foundation, Division of Atmospheric Sciences (ATM-9711076 and ATM-01123454) and by the Office of Naval Research (ONR) program element 0601153N. The simulations were made using the Advanced Regional Prediction (ARPS) developed by the Center for Analysis and Prediction of Storms (CAPS), University of Oklahoma. CAPS is supported by the National Science Foundation and the Federal Aviation Administration. The computing was done on a SGI Origin 200 machine at the Yale Center for Earth Observation.

REFERENCES

Baines, P. G. and Smith, R. B. 1993. Upstream stagnation points in stratified flow past obstacles. *Dyn. Atmos. Oceans* **18**, 105–113.

Barcilon, A. and Fitzjarrald, D. 1985. A nonlinear steady model for moist hydrostatic mountain waves. *J. Atmos. Sci.* **42**, 58–67.

Barcilon, A., Jusem, J. C. and Drazin, P. G. 1979. On the two-dimensional hydrostatic flow of a stream of moist air over a mountain ridge. *Geophys. Astrophys. Fluid Dynam.* **13**, 125–140.

Bauer, M. H., Mayr, G. J., Vergeiner, I. and Pichler, H. 2000. Strongly nonlinear flow over and around a three-dimensional mountain as a function of the horizontal aspect ratio. *J. Atmos. Sci.* **57**, 3971–3991.

Carbone, R. E., Cooper, W. A. and Lee, W. 1995. Forcing of flow reversal along the windward slopes of Hawaii. *Mon. Wea. Rev.* **123**, 3466–3480.

Colton, D. E. 1976. Numerical simulation of the orographically induced precipitation distribution for use in hydrologic analysis. *J. Appl. Meteorol.* **15**, 1241–1251.

Cotton, W. R. and Anthes, R. A. 1989. *Storm and cloud dynamics*. Academic Press, New York, 881 pp.

Durran, D. and Klemp, J. 1982a. The effects of moisture on trapped mountain lee waves. *J. Atmos. Sci.* **39**, 2152–2158.

Durran, D. and Klemp, J. 1982b. On the effects of moisture on the Brunt-Vaisala frequency. *J. Atmos. Sci.* **39**, 2152–2158.

Durran, D. and Klemp, J. 1983. A compressible model for the simulation of moist mountain waves. *Mon. Wea. Rev.* **111**, 2341–2361.

Ferretti, R., Low-Nam, S. and Rotunno, R. 2000. Numerical simulations of the Piedmont flood of 4–6 November 1994. *Tellus* **52A**, 168–180.

Fraser, A. B., Easter, R. C. and Hobbs, P. V. 1973. A theoretical study of the flow of air and fallout of solid precipitation over mountainous terrain. Part I: Airflow model. *J. Atmos. Sci.* **30**, 801–812.

Hunt, C. R. and Snyder, W. H. 1980. Experiments on stably and neutrally stratified flow over a model three-dimensional hill. *J. Fluid. Mech.* **96**, 671–704.

Huppert, H. E. and Miles, J. W. 1969. Lee waves in a stratified flow: Part 3. Semi-elliptical obstacles. *J. Fluid Mech.* **35**, 481–496.

Jiang, Q. 2000. Some theoretical aspects of orographic precipitations. Ph.D. Thesis, Yale University.

Jiang, Q. and Smith, R. B. 2003. Cloud timescales and orographic precipitation. *J. Atmos. Sci.*, in press.

Katzfey, J. J. 1995. Simulation of extreme New Zealand precipitation events. Part II: Mechanisms of precipitation development. *Mon. Wea. Rev.* **123**, 755–775.

Lalas, D. P. and Einaudi, F. 1974. On the correct use of the wet adiabatic lapse rate in the stability criteria of a saturated atmosphere. *J. Appl. Meteorol.* **13**, 318–324.

Lin, Y. L., Farley, R. D. and Orville, H. D. 1983. Bulk parameterization of the snow field in a cloud model. *J. Clim. Appl. Meteorjol.* **22**, 1065–1092.

Marwitz, J. 1980. Winter storms over the San Juan Mountains, Part. 1: Dynamical processes. *J. Appl. Meteorol.* **19**, 913–926.

Ólafsson, H. and Bougeault, P. 1996. Nonlinear flow past an elliptic mountain ridge. *J. Atmos. Sci.* **53**, 2465–2489.

Rhea, J. O. 1978. Ph. D. Thesis, Atm. Sci. Paper No. 287, Colorado State University, 198 pp.

Rotunno, R. and Ferretti, R. 2001. Mechanisms of intense alpine rainfall. *J. Atmos. Sci.* **58**, 1732–1749.

Sanberg, J. A. M. and Oerlemans, J. 1983. Modeling of Pleistocene European ice sheets: the effect of upslope precipitation. *Geologie en Mijnbouw* **62**, 267–273.

Sheppard, P. A. 1956. Airflow over mountains. *Q. J. R. Meteorol. Soc.* **82**, 528.

Sinclair, M. R. 1994. A diagnostic model for estimating orographic precipitation. *J. Appl. Meteorol.* **33**, 1163–1175.

Smith, R. B. 1979. The influence of mountains on the atmosphere. *Adv. Geophys.* **21**, 87–230.

Smith, R. B. 1989. Mountain-induced stagnation points in hydrostatic flow. *Tellus* **41A**, 270–274.

Smith, R. B. and Lin, Y. L. 1982. The addition of heat to a stratified air stream with application to the dynamics of orographic rain. *Q. J. R. Meteorol. Soc.* **108**, 353–379.

Smith, R. B. and Grønås, S. 1993. Stagnation points and bifurcation in 3-D mountain airflow. *Tellus* **45A**, 28–43.

Smolarkiewicz, P. K. and Rotunno, R. 1989. Low Froude number flow past three dimensional obstacles. Part I: Baroclinically generated lee vortices. *J. Atmos. Sci.* **46**, 1154–1164.

Smolarkiewicz, P. K. and Rotunno, R. 1990. Low Froude number flow past three-dimensional obstacles. Part II: Upwind flow reversal zone. *J. Atmos. Sci.* **47**, 1498–1511.

Xue, M., Droegemeier, K. K., Wong, V., Shapiro, A. and Brewster, K. 1995. ARPS Version 4.0 User's Guide. Center for Analysis and Prediction of Storms, 380 pp.